

NASA Contractor Report

## THERMOSOLUTAL CONVECTION AND MACROSEGREGATION IN DENDRITIC ALLOYS

D.R. Poirier and J.C. Heinrich  
*The University of Arizona*  
*Tucson, Arizona*

September 1993

Prepared for  
Lewis Research Center  
Under Grant NAG3-1060

(NASA-CR-194039) THERMOSOLUTAL  
CONVECTION AND MACROSEGREGATION IN  
DENDRITIC ALLOYS Final Technical  
Report (Arizona Univ.) 52 p

N94-12825

Unclass

G3/26 0185523

# THERMOSOLUTAL CONVECTION AND MACROSEGREGATION IN DENDRITIC ALLOYS

D.R. Poirier and J.C. Heinrich  
The University of Arizona  
College of Engineering and Mines  
Tucson, Arizona 85721

A mathematical model of solidification, that simulates the formation of channel segregates or freckles, is presented. The model simulates the entire solidification process, starting with the initial melt to the solidified cast, and the resulting segregation is predicted. Emphasis is given to the initial transient, when the dendritic zone begins to develop and the conditions for the possible nucleation of channels are established. The mechanisms that lead to the creation and eventual growth or termination of channels are explained in detail and illustrated by several numerical examples.

A finite element model is used for the simulations. It uses a single system of equations to deal with the all-liquid region, the dendritic region, and the all-solid region. The dendritic region is treated as an anisotropic porous medium. The algorithm uses the bilinear isoparametric element, with a penalty function approximation and a Petrov-Galerkin formulation.

The major task was to develop the solidification model. In addition, this report briefly describes other tasks that were performed in conjunction with the modelling of dendritic solidification.

## NOMENCLATURE

$a$	random number
$\bar{C}$	average total concentration of solute
$\hat{c}$	heat capacity
$C_l$	concentration of solute in the liquid
$C_L$	interdendritic solute concentration from the liquidus line in the phase diagram
$\bar{C}_s$	local solute concentration in the solid
$C_\infty$	reference solute concentration (concentration in the liquid before solidification)
$d_1$	primary dendrite arm spacing
$D$	solute diffusivity in the liquid
$Da_x, Da_z$	Darcy number in the $x$ and $z$ direction, respectively
$g$	gravitational acceleration
$G$	reference thermal gradient
$h$	local mesh length in the direction of flow
$H$	reference length
$H_T$	$z$ coordinate for the top of the container
$I$	auxiliary variable for total solute concentration in the solid
$k$	partition ratio
$K_x, K_z$	permeability in the $x$ and $z$ direction, respectively
$L$	latent heat
$\bar{L}, \hat{L}$	first and second nondimensional latent heat, respectively
$m$	slope of the liquidus line in the phase diagram
$n$	unit outward normal vector
$N_i$	shape function
$p$	pressure
$p_s$	hydrostatic pressure
$P_i$	Petrov-Galerkin perturbation function
$Pr$	Prandtl number
$q$	prescribed boundary heat flux
$r$	cooling rate prescribed at $z = 0$
$R_s, R_T$	solutal and thermal Rayleigh number, respectively
$Sc$	Schmidt number
$t$	time
$T$	temperature
$T_E$	eutectic temperature
$T_i$	initial temperature
$T_L$	liquidus temperature
$T_0$	reference temperature
$\Delta t$	time step
$u$	$x$ component of the superficial velocity
$u_p$	$x$ component of the pore velocity
$U$	reference velocity

$u$	magnitude of liquid velocity
$V$	solidification velocity
$w$	$z$ component of the superficial velocity
$w_p$	$z$ component of the pore velocity
$W$	width of the container
$W_i^k$	Petrov-Galerkin weighting function
$x, z$	coordinates
$\alpha$	thermal diffusivity
$\alpha_k$	Petrov-Galerkin coefficients
$\beta_T, \beta_S$	thermal and solutal expansion coefficient, respectively.
$\gamma_1$	cell Reynolds number
$\gamma_2, \gamma_3$	cell Péclet number in the energy and solute concentration equation, respectively
$\Gamma$	domain boundary
$\epsilon$	convergence tolerance
$\theta$	angle of the gravity vector with respect to the $x$ axis
$\lambda$	penalty parameter
$\nu$	kinematic viscosity
$\rho$	density
$\rho_0$	reference density
$\tau$	reference time
$\phi$	volume fraction of interdendritic liquid
$\Omega$	global domain

## TABLE OF CONTENTS

SUMMARY .....	i
NOMENCLATURE .....	ii
I. INTRODUCTION .....	1
II. SOLIDIFICATION MODEL .....	3
III. CALCULATION STRATEGY .....	8
A. Remelting .....	10
B. Energy Equation .....	10
C. Solidification at Eutectic Temperature .....	12
D. Time Step and Mesh Size .....	13
IV. FINITE ELEMENT METHOD .....	15
V. NUMERICAL RESULTS .....	22
VI. DISCUSSION .....	28
VII. CONCLUSIONS .....	31
VIII. OTHER ACCOMPLISHMENTS .....	32
APPENDIX - Functions Used for Permeability .....	33
REFERENCES .....	35
ACKNOWLEDGMENTS .....	39

## I. INTRODUCTION

An increasing number of technological applications requires the operation of critical mechanical components under severe conditions of high temperatures and stresses. If improperly manufactured, these components are subject to creep fracture and thermal fatigue failures, which are almost always associated with grain boundaries that are transverse to the applied stress. The modern day directional solidification technique provides an effective means of controlling the grain shape, producing a columnar microstructure with all the grain boundaries running in the longitudinal direction of the casting. This greatly improves material performance at elevated temperatures. Still better properties can be obtained by casting a single crystal (i.e., a dendritic monocrystal), in which only one columnar grain is allowed to grow and form the main body of the casting [1].

Without proper control, directionally solidified castings are not free of defects. Particularly troublesome are localized segregates at the macroscopic scale, which are found in many directionally solidified (DS) alloys, including some superalloys. These segregates are observed as long and narrow trails, aligned parallel to the direction of gravity in DS castings, and are enriched in the normally segregating elements and depleted of the inversely segregating elements, *i.e.*, their composition is shifted toward the eutectic composition. In horizontally solidified ingots of steel similar defects are known as "A" segregates, while in DS castings they have a more pronounced channel shape and are termed "freckles." This non-uniformity of composition is highly undesirable because the resulting variation in physical properties within the casting can lead to inferior performance of the components

manufactured from the casting. In ingot production, an excessive number of defects can require a large amount of cropping, at a considerable cost of energy and material.

Many analytical and experimental works have been done in the recent years in order to observe, explain and prevent the formation of both "A" segregates [2-4] and freckles [5-13] in directionally solidified alloys. This paper addresses the latter type of defects, *i.e.*, freckles when an alloy is cooled from below.

The opacity of metals prevents direct observation of the nucleation and growth of channels during solidification. Observations are usually done by quenching the ingot at different stages of solidification and analyzing the solidified macrostructure. Much of what is known about channel dynamics has been learned from the transparent analogue  $\text{NH}_4\text{Cl}$ - $\text{H}_2\text{O}$  system [5,8]. Here, it is clearly seen that freckles are a direct consequence of upward flowing liquid jets that emanate from within the mushy zone. In the case of a binary alloy this requires that the solute be less dense than the solvent if it segregates normally or more dense if it segregates inversely.

Because a density inversion also occurs in metallic systems where freckles are observed, it was proposed by Copley *et al.* [5], and further supported in later works [4,6,7,8,11,14], that buoyancy driven convection is responsible for channel segregation. Although the influence of buoyancy effects in segregation seems to be evident, the large differences in thermal conductivities, solid-liquid densities and, in particular, the fraction of liquid in the dendritic structure can lead to a convection pattern that is very different from that observed in the water-based mixtures, as it has been reported in experiments using

radioactive tracer techniques [14,15] and in an analytical model of thermosolutal convection in dendritic alloys [16].

Solidification simulation is motivated by the need to understand the basic mechanisms of the segregation of alloy components. The earliest works considered only the solute conservation equation [17-19]. Soon thereafter, natural convection of the interdendritic liquid [20-22] and in the all-liquid region [23] were studied. Thermosolutal convection, however, was not considered, so early models were not capable of predicting thermosolutal instabilities at the solidifying interface that result in segregation defects in solidified alloys.

Models that incorporate the effect of thermosolutal convection have been developed by other researchers as well, e.g., Bennon and Incropera [3,24-26], and Beckermann and Viskanta [27-28] simulated horizontal solidification of aqueous solutions of ammonium chloride.

In our work, we have used a finite element algorithm to calculate macrosegregation and the formation of channels and freckles in Pb-Sn alloys. The algorithm has also been used to reproduce a calculation for horizontal solidification of an  $\text{NH}_4\text{Cl-H}_2\text{O}$  solution presented in Ref. [3]. Calculations presented herein show that the present model is capable of capturing the formation of channels and freckles during vertical solidification of alloys.

## II. SOLIDIFICATION MODEL

We consider an alloy melt undergoing directional solidification under the following basic assumptions:

1. Only solid and liquid phases may be present, i.e., no pores form.



2. The flow is two dimensional and laminar, and the solid phase is stationary.
3. The solid and liquid phases have equal thermal properties and densities.
4. There is no diffusion of solute in the solid phase.
5. The thermal properties are constant, and the Boussinesq approximation is made; hence, the density is constant except in the body force term of the momentum equations.
6. The dendritic region (often called the mushy zone) is treated as a porous medium with anisotropic permeability where the fluid velocities are the superficial velocity components.

With these assumptions, the basic nondimensional equations of momentum, continuity, energy, and solute transport can be written [29] as

$$\begin{aligned} \text{Pr} \frac{\partial u}{\partial t} + \frac{1}{\phi} \left[ u \frac{\partial u}{\partial x} + w \frac{\partial u}{\partial z} \right] = & - \phi \frac{\partial p}{\partial x} + \text{Pr} \left[ \frac{\partial^2 u}{\partial x^2} + \frac{\partial^2 u}{\partial z^2} \right] \\ & - \phi \frac{\text{Pr}}{\text{Da}_x} u - \phi \cos \theta \text{Pr} \left[ R_T T + \frac{R_s}{\text{Sc}} (C_l - 1) \right] \end{aligned} \quad (1)$$

$$\begin{aligned} \text{Pr} \frac{\partial w}{\partial t} + \frac{1}{\phi} \left[ u \frac{\partial w}{\partial x} + w \frac{\partial w}{\partial z} \right] = & - \phi \frac{\partial p}{\partial z} + \text{Pr} \left[ \frac{\partial^2 w}{\partial x^2} + \frac{\partial^2 w}{\partial z^2} \right] \\ & - \phi \frac{\text{Pr}}{\text{Da}_z} w - \phi \sin \theta \text{Pr} \left[ R_T T + \frac{R_s}{\text{Sc}} (C_l - 1) \right] \end{aligned} \quad (2)$$

$$\frac{\partial u}{\partial x} + \frac{\partial w}{\partial z} = 0 \quad (3)$$

$$\text{Pr} \frac{\partial T}{\partial t} + u \frac{\partial T}{\partial x} + w \frac{\partial T}{\partial z} = \frac{\partial^2 T}{\partial x^2} + \frac{\partial^2 T}{\partial z^2} - \bar{L} \frac{\partial \phi}{\partial t} \quad (4)$$

$$\text{Pr} \frac{\partial \bar{C}}{\partial t} + u \frac{\partial C_l}{\partial x} + w \frac{\partial C_l}{\partial z} = \frac{\text{Pr}}{\text{Sc}} \left[ \frac{\partial}{\partial x} \phi \frac{\partial C_l}{\partial x} + \frac{\partial}{\partial z} \phi \frac{\partial C_l}{\partial z} \right] \quad (5)$$

The variables are defined in the nomenclature.

In the mushy zone, where  $\phi < 1$ , we use  $u$  and  $w$  as the superficial velocities, *i.e.*,

$$u = \phi u_p \quad w = \phi w_p \quad (6)$$

where  $u_p$  and  $w_p$  are the components of the pore velocity.

The nondimensional numbers are defined by  $\text{Pr} = \nu/\alpha$ ,  $\text{Da}_x = K_x/H^2$ ,  $\text{Da}_z = K_z/H^2$ ,  $\text{R}_T = (\beta_T g G H^4)/\nu\alpha$ ,  $\text{R}_S = (\beta_S g C_\infty H^3)/\nu D$ ,  $\text{Sc} = \nu/D$ , and  $\bar{L} = L/\hat{c}GH$ . Note that  $H$  is the reference length,  $G$  is a reference thermal gradient, and  $C_\infty$  is the reference concentration.

Implicit in Eqs. (1) and (2) is a constitutive relation of the form

$$\rho = \rho_0 [1 - \beta_T (T - T_0) - \beta_S (C - C_\infty)] \quad (7)$$

in the body force terms, where  $\rho_0$  and  $T_0$  are reference density and temperature, respectively, and  $C_\infty$ , the reference solute concentration, is the concentration in the liquid before solidification. The nondimensionalization given above also uses a reference velocity  $U = \alpha/H$ , a reference time  $\tau = H^2/\nu$ , and a reference pressure  $\rho_0 U^2$ . The temperature and solute concentration in the liquid are nondimensionalized using  $(T - T_0)/GH$  and  $C_l/C_\infty$ , respectively, and the total solute concentration by  $\bar{C}/C_\infty$ .

The momentum equations above are similar to the ones used by Beckermann and Viskanta [27-28], but differ from the ones used by Bennon and Incropera [3,24-26]. Readers are referred to Ganesan and Poirier [30] and Nandapurkar *et al.* [31] for more details pertaining to the momentum equations.

To complete the model, we require a relation between the total solute concentration  $\bar{C}$  and the solute concentration in the liquid  $C_l$  of the form

$$\bar{C} = \phi C_l + (1 - \phi) \bar{C}_s \quad (8)$$

where  $\bar{C}_s$  is the average local solute concentration in the solid. The model allows for microsegregation in the solid; hence,  $\bar{C}_s$  is not uniform but is given by

$$\bar{C}_s = \frac{1}{1-\phi} \int_{\phi}^1 k C_l d\phi \quad (9)$$

where  $k$  is the equilibrium partition ratio defined as the ratio of the concentration of solute at the solid dendritic interface to the solute concentration in the interdendritic liquid. In this work, we assume  $k$  is constant.

At a given temperature in the mushy zone, the composition of the interdendritic liquid is nearly uniform, and the local liquid-solid interface is very near equilibrium [32]; hence, the composition of the interdendritic liquid is given by the liquidus line in the phase diagram of the alloy. Consequently,

$$C_l = C_L(T) \text{ (liquidus line in the phase diagram)} \quad \phi < 1$$

$$C_l = \bar{C} \quad \phi = 1$$

and Eq. (8) can be used to calculate the local volume fraction of liquid,  $\phi$ .

In this work, we present two-dimensional simulations in rectangular domains (Fig. 1). The boundary conditions associated with Eqs. (1) and (2) are no-slip at solid boundaries; *i.e.*,  $u = w = 0$  at solid boundaries that include completely solidified regions in the domain. For solidification in a very tall container, the normal stresses along the top boundary are zero; *viz.*,

$$\frac{\partial u}{\partial z} + \frac{\partial w}{\partial x} = 0 \quad 2 \text{ Pr} \frac{\partial w}{\partial z} = \phi p \quad z = H_T \quad (11)$$

If we want the upper boundary to be a free surface, we assume that the surface is undeformable. The boundary conditions are then

$$\frac{\partial u}{\partial z} = w = 0 \quad z = H_T \quad (12)$$

The boundary conditions for temperature along any of the walls can be of two types: a prescribed heat flux,

$$-\rho_0 \hat{c} \alpha \frac{\partial T}{\partial n} = q \quad (13)$$

(along the boundary), where  $\partial/\partial n$  denotes the normal derivative in the direction of the outward unit normal to the boundary and  $q$  is the prescribed heat flux along that boundary; or a prescribed temperature written as

$$T = T_i - rt \quad (14)$$

(along the boundary), where  $T_i$  is the initial temperature and  $r$  is a prescribed cooling rate. Any combination of the above-cited conditions can be imposed along the boundaries of the domain.

No transfer of solute mass is allowed at solid boundaries or at an undeformable free surface (it is assumed at the top of the container), *i.e.*,

$$\phi \frac{\partial C_l}{\partial n} = 0 \quad (15)$$

along those boundaries. If the assumption of a very long container is made, we must require a balance of diffusive and convective transport along that boundary so that

$$D \frac{\partial C_l}{\partial x} + w(C_l - C_\infty) = 0 \quad (16)$$

at the top boundary.

### III. CALCULATION STRATEGY

We adopt a strategy in which the equations are solved sequentially and an iteration is performed to achieve convergence at each time step. First, we combine Eqs. (8) and (9) and obtain

$$\bar{C} = \phi C_l + I \quad (17)$$

where  $I$  is the integral in Eq. (9).

To advance from time  $t_n$ , at which all conditions are known, to time  $t_{n+1} = t_n + \Delta t$ , the following steps are taken, where the dependent variables are computed using the latest available values of all other variables on which they depend.

1. At time  $t_n$ , parameters  $u_n$ ,  $w_n$ ,  $T_n$ , *etc.*, are known.

2. Advance to time step  $t_{n+1} = t_n + \Delta t$ . Set  $i = 0$ ,  $u_{n+1}^{i=0} = u_n$ ,  $w_{n+1}^{i=0} = w_n$ ,  $T_{n+1}^{i=0} = T_n$ , etc., where  $i$  is an iteration index and the subindex denotes the time level.

3. Compute  $u_{n+1}^{i+1}$  and  $w_{n+1}^{i+1}$  from Eqs. (1)-(3) and (7).

4. Compute  $T_n^{i+1}$  from Eq. (4).

5. From Eq. (10), set

$$\begin{aligned} C_{l_{n+1}}^{i+1} &= C_L(T_{n+1}^{i+1}) & C_{l_{n+1}}^i &\leq C_L(T_{n+1}^{i+1}) \\ C_{l_{n+1}}^{i+1} &= \bar{C}_{n+1}^i & C_{l_{n+1}}^i &> C_L(T_{n+1}^{i+1}) \end{aligned} \quad (18)$$

6. Calculate  $\phi_{n+1}^{i+1}$  from Eq. (17) in the form

$$\phi_{n+1}^{i+1} = \frac{\bar{C}_{n+1}^i - I_{n+1}^i}{C_{l_{n+1}}^{i+1}} \quad (19)$$

7. For nodes where  $0 < \phi_{n+1}^{i+1} < 1$ , compute  $I_{n+1}^{i+1}$ .

8. Compute  $\bar{C}_{n+1}^{i+1}$  using Eq. (5).

9. Recalculate  $\phi_{n+1}^{i+1}$  using Eq. (19).

10. If  $\|\phi_{n+1}^{i+1} - \phi_{n+1}^i\| < \epsilon$  (tolerance), then

$$u_{n+1} = u_{n+1}^{i+1}, \quad w_{n+1} = w_{n+1}^{i+1}, \quad T_{n+1} = T_{n+1}^{i+1}, \quad \text{etc.}; \quad n = n + 1; \quad \text{go to step 2.}$$

Otherwise, set  $i = i + 1$  and go to step 4. (Here,  $\| / \|$  denotes the Euclidean norm.)

Steps 4-10 are repeated iteratively during each time step until convergence of  $\phi$  is achieved. The velocities are calculated only once per time step because they have negligible sensitivity to small changes in the rest of the dependent variables [29]. At the end of each time step, the average concentration in the solid  $\bar{C}_S$  is calculated from Eq. (9).

#### A. Remelting

The integral  $I$  in Eq. (17) is computed incrementally by adding the increment corresponding to a change in  $\phi$  to the previous value of  $I$ . The increment can be positive or negative, depending on whether the material undergoes solidification or remelting. More details can be found in Ref. [33]. If solidification has occurred and the increment is positive,  $I$  is calculated directly. If there is remelting, however,  $I$  must be obtained from the solidification history, with values of  $\phi$  and  $I$  saved from the previous time steps. To alleviate the excessive amount of storage required,  $\phi$  and  $I$  are not saved at every time step. Instead,  $I$  is stored at increments of  $\Delta\phi = 0.01$ , and linear interpolation is used for other values of  $\phi$ .

#### B. Energy Equation

A simple analysis shows that the algorithm for calculating the temperature and the volume fraction liquid is only conditionally stable and, unfortunately, stability only holds for values of latent heat that are much smaller than in metallic alloys. In order to obtain a stable algorithm, the energy equation, Eq. (4), was reformulated to make the latent heat term

implicit. To eliminate  $\phi$  from Eq. (4), we first differentiate Eq. (17) with respect to time, yielding

$$\frac{\partial \bar{C}}{\partial t} = \phi \frac{\partial C_l}{\partial t} + C_l \frac{\partial \phi}{\partial t} + \frac{\partial I}{\partial t} \quad (20)$$

If we approximate the liquidus line by a straight line with slope  $m$  ( $m < 0$ ), the temperature is related to the solute concentration in the interdendritic liquid by

$$T = T_M + \hat{m} C_l \quad (21)$$

where  $T_M$  is the melting point of the solvent and  $\hat{m} = mC_0/GH$ . Equations (5), (20), and (21) can then be combined with Eq. (4) to give

$$\begin{aligned} \left[ \text{Pr} - \frac{\hat{L}\phi}{C_l} \right] \frac{\partial T}{\partial t} + \left[ 1 - \frac{\hat{L}}{\text{Pr}C_l} \right] \left[ u \frac{\partial T}{\partial x} + w \frac{\partial T}{\partial z} \right] &= \frac{\partial^2 T}{\partial x^2} + \frac{\partial^2 T}{\partial z^2} \\ - \left[ \frac{\hat{L}}{\text{Sc}C_l} \right] \left[ \frac{\partial}{\partial x} \left[ \phi \frac{\partial T}{\partial x} \right] + \frac{\partial}{\partial z} \left[ \phi \frac{\partial T}{\partial z} \right] \right] &+ \frac{\bar{L}}{C_l} \frac{\partial I}{\partial t} \end{aligned} \quad (22)$$

where  $\hat{L}$  is the second nondimensional latent heat defined as  $\hat{L}_1 = L/m\hat{c}C_0$ . Note that when remelting occurs, we cannot make the assumption that  $\partial/\partial t[\int_{\phi} kC_l d\phi] = -kC_l \partial\phi/\partial t$ , as was done, for example, in Ref. [17]. An explanation of this point is given by Felicelli [29] and by Felicelli *et al.* [33].

The fact that Eq. (22) rather than Eq. (4) must be used to calculate the temperature introduces a computational inconvenience because Eq. (22) is nonlinear and must be reconstructed and solved again at every time step, increasing the CPU time significantly. It must also be pointed out that Eq. (21) is not uniformly valid throughout the domain because



it does not reduce to Eq. (4) when  $\phi = 1$ . Therefore, the terms containing  $\hat{L}$  apply only to the elements in the mushy zone, where  $C_l = C_L(T)$ .

### C. Solidification at Eutectic Temperature

Binary alloys solidify over a range of temperatures, and the temperature is governed by the energy equation, Eq. (4). If we look back at the computational strategy, the algorithm proceeds as follows:

1. A decrease in the temperature of a volume element in the mushy zone automatically results in an increase in the solute concentration in the interdendritic liquid, which is given by Eq. (18).
2. An increase in the concentration in the interdendritic liquid produces a decrease in the volume fraction of liquid according to Eq. (19).

This means that the temperature is the variable that drives the solidification process. When a volume element reaches the eutectic temperature, however, the remaining fraction of interdendritic liquid solidifies at constant temperature, assuming no undercooling of the eutectic reaction. Consequently, at this point the solidification algorithm must be modified. In formulations based on enthalpy, such as the one used by Bennon and Incropera [24-26], the enthalpy is still valid at the eutectic temperature.

In some ways, enthalpy formulations are convenient, but they require a transformation to obtain the temperature. Unfortunately, an algebraic transformation relating enthalpy to temperature is only possible for simple thermophysical descriptions, such as constant specific heat and complete diffusion in the solid. The assumption of complete diffusion in the solid

yields a direct relation between  $\phi$  and  $T$  that, when combined with the additional assumption of linear dependence of the phase enthalpies with temperature, yields an algebraic equation for the temperature as a function of the mixture's enthalpy. This property was exploited by Bennon and Incropera [3], who used an enthalpy-based energy equation.

In order to retain the temperature formulation, an alternative is followed to solve for solidification at constant temperature. When a node in the domain reaches the eutectic temperature, the energy equation, Eq. (4), is used to calculate the volume fraction of liquid while setting the time derivative of  $T$  equal to zero to effect solidification at constant temperature. Equation (4) becomes

$$\frac{\partial \phi}{\partial t} = \frac{1}{L} \left[ \frac{\partial^2 T}{\partial x^2} + \frac{\partial^2 T}{\partial z^2} - u \frac{\partial T}{\partial x} - w \frac{\partial T}{\partial z} \right] \quad (23)$$

Equation (23) is solved only at the points solidifying at constant temperature; the complete energy equation is solved elsewhere. Physically, the eutectic isotherm advances smoothly through the domain; that is, a coordinate does not stay at the eutectic temperature for a finite period of time. The present model, however, treats volume-averaged quantities in a porous medium, so a volume element or nodal point stays at constant temperature until it is completely solidified. After that, its temperature is calculated with Eq. (4), which reduces to the conduction equation in the solid.

#### D. Time Step and Mesh Size

If thermosolutal effects are important, the relevant length scale to be resolved is  $D/V$ , where  $V$  is a characteristic solidification speed. For the system under consideration, *i.e.*,

slowly solidifying Pb-Sn alloys; this length scale is typically of the order of  $300\ \mu\text{m}$  and requires a very fine mesh spacing in the vertical direction. In the horizontal direction, channels in the mushy zone can be narrow, comparable to the order of  $D/V$ . Finally, we work with uniform meshes because the location at which channels form cannot be predicted *a priori*; as a result, calculations are limited to the rather small domains.

A second consideration for selecting the spatial resolution is that there be enough nodes to adequately resolve the distribution of the volume fraction of liquid  $\phi$  in the mushy zone. This consideration is discussed later in relation to the mesh spacings used in the calculated results.

The choice of the time step is more complicated because of the nonlinear nature of the problem and the need to satisfy several stability constraints in the calculations. So far, the calculations are performed using a constant time step; hence, the most stringent of the following stability criteria must be satisfied.

1. The convective terms are treated explicitly in Eqs. (1), (2), and (4), so the stability condition of the form  $\Delta t_1 \leq (|u|/\Delta x + |w|/\Delta z)^{-1}$  applies everywhere in the computational mesh.
2. The explicit treatment of the body force terms gives  $\Delta t_2 \leq (R_T + R_S/Sc)^{-1}$ .
3. A third consideration can be added, namely, that it is more efficient to choose a time step for which no more than three iterations are needed for convergence within the time step.

The above criteria are not optimal bounds. However, choosing  $\Delta t \leq \min(\Delta t_1, \Delta t_2)$  gives a good estimate. An added difficulty is that  $\Delta t_1$  can vary significantly as the

solidification proceeds. Hence careful monitoring of the flow field is required to avoid an overly conservative time step.

#### IV. FINITE ELEMENT METHOD

The computational algorithm makes use of a standard penalty function formulation because the pressure is not needed. The pressure in Eqs. (1) and (2) is eliminated using the pseudo-constitutive relation

$$p = p_s - \lambda \left[ \frac{\partial u}{\partial x} + \frac{\partial w}{\partial z} \right] \quad (24)$$

where  $p_s$  is the hydrostatic pressure and  $\lambda$  is a large "penalty" parameter. This method has been discussed in detail by Marshall *et al.* [34], Heinrich and Marshall [35], and Heinrich and Yu [36] in the context of buoyancy-driven flows. Theoretical aspects have been studied by Oden [37]. Equation (24) is substituted into Eqs. (1) and (2), and the continuity equation, Eq. (3), is eliminated. As a result, the pressure is not calculated but, if needed, it can be recovered *a posteriori* by solving a Poisson equation (see [38, 39]).

The present scheme is based on the bilinear Lagrangian isoparametric element. The convective terms are dealt with using a Petrov-Galerkin formulation in which the weighting function is perturbed in the convective term. If we denote the shape function corresponding to node  $i$  by  $N_i$ , the perturbed weighting function takes the form

$$W_i^K = N_i + \alpha_K P_i \quad K = 1, 2, 3, \quad (25)$$

where  $K = 1$  corresponds to Eqs. (1) and (2),  $K = 2$  to Eq. (22), and  $K = 3$  to Eq. (5).

The parameters  $\alpha_K$  are given by

$$\alpha_K = \coth \gamma_K - \frac{1}{\gamma_K} \quad (26)$$

where

$$\gamma_1 = \frac{\nu h}{2\phi \text{Pr}} \quad (27)$$

is the cell Reynolds number,

$$\gamma_2 = \frac{\nu h[1 - (\hat{L}/\text{Pr } C_l)]}{2[1 + (\hat{L}\phi/\text{Sc } C_l)]} \quad (28)$$

is the energy cell Péclet number,

$$\gamma_3 = \frac{\text{Sc } \nu h}{2\phi \text{Pr}} \quad (29)$$

is the solute concentration cell Péclet number,  $\nu = |\sqrt{u^2 + w^2}|$  is the local fluid speed, and  $h$  is the local element length in the direction of flow. Details on calculating  $h$  are given in Ref. [36].

Denoting the domain by  $\Omega$  and its boundary by  $\Gamma$ , the weak forms of Eqs. (1) and (2) are

$$\begin{aligned} & \int_{\Omega} \left\{ N_i \text{Pr} \frac{\partial u}{\partial t} + \lambda \phi \frac{\partial N_i}{\partial x} \left[ \frac{\partial u}{\partial x} + \frac{\partial w}{\partial z} \right] + \text{Pr} \left[ \frac{\partial N_i}{\partial x} \frac{\partial u}{\partial x} + \frac{\partial N_i}{\partial z} \frac{\partial u}{\partial z} \right] + N_i \frac{\text{Pr} \phi}{\text{Da}_x} u \right\} d\Omega \\ & = - \int_{\Omega} \left\{ W_i^1 \frac{1}{\phi} \left[ u \frac{\partial u}{\partial x} + w \frac{\partial u}{\partial z} \right] + N_i \phi \cos \theta \text{Pr} \left[ R_T T + \frac{R_s}{\text{Sc}} (C_l - 1) \right] \right\} d\Omega \end{aligned} \quad (30)$$

and

$$\begin{aligned}
& \int_{\Omega} \left\{ N_i \text{Pr} \frac{\partial w}{\partial t} + \lambda \phi \frac{\partial N_i}{\partial x} \left[ \frac{\partial u}{\partial x} + \frac{\partial w}{\partial z} \right] + \text{Pr} \left[ \frac{\partial N_i}{\partial x} \frac{\partial u}{\partial x} + \frac{\partial N_i}{\partial z} \frac{\partial w}{\partial z} \right] + N_i \frac{\text{Pr} \phi}{\text{Da}_z} w \right\} d\Omega \\
& = - \int_{\Omega} \left\{ W_i^1 \frac{1}{\phi} \left[ u \frac{\partial u}{\partial x} + w \frac{\partial w}{\partial z} \right] + N_i \phi \sin \theta \text{Pr} \left[ R_T T + \frac{R_S}{\text{Sc}} (C_l - 1) \right] \right\} d\Omega
\end{aligned} \tag{31}$$

where the left-hand sides are treated implicitly and the right-hand sides are evaluated explicitly with the latest values of the dependent variables. All variables are interpolated using the bilinear isoparametric shape functions; *i.e.*, for a generic function  $f(x, z)$  we write

$$f(x, z) = \sum_i N_i(x, z) f_i \tag{32}$$

where  $i$  ranges over the number of nodes in the mesh and  $f_i \equiv f(x_i, z_i)$  is the value of the function at node  $i$ .

The weak form of the energy equation, Eq. (22), is

$$\begin{aligned}
& \int_{\Omega} \left\{ N_i \left[ \text{Pr} - \frac{\hat{L}\phi}{C_l} \right] \frac{\partial T}{\partial t} - \left[ 1 - \frac{\hat{L}\phi}{\text{Sc} C_l} \right] \left[ \frac{\partial N_i}{\partial x} \frac{\partial T}{\partial x} + \frac{\partial N_i}{\partial z} \frac{\partial T}{\partial z} \right] \right. \\
& \quad \left. + \frac{\hat{L}\phi N_i}{\text{Sc} C_l^2} \left[ \frac{\partial C_l}{\partial x} \frac{\partial T}{\partial x} + \frac{\partial C_l}{\partial z} \frac{\partial T}{\partial z} \right] \right\} d\Omega \\
& = \int_{\Omega} \left[ W_i^2 \left[ \frac{\hat{L}}{\text{Pr} C_l} - 1 \right] \left[ u \frac{\partial T}{\partial x} + w \frac{\partial T}{\partial z} \right] + N_i \frac{\bar{L}}{C_l} \frac{\partial I}{\partial t} \right] d\Omega \\
& \quad + \int_{\Gamma} N_i \left[ 1 - \frac{\hat{L}\phi}{\text{Sc} C_l} \right] \frac{\partial T}{\partial n} D\Gamma
\end{aligned} \tag{33}$$

In Eq. (33), the line integral is taken only over those portions of the boundary where a flux condition as given by Eq. (13) is prescribed.

The weak form for the solute concentration equation is given by

$$\begin{aligned} & \int_{\Omega} \text{Pr } N_i \frac{\partial \bar{C}}{\partial t} d\Omega + \int_{\Omega} \frac{\text{Pr } \phi}{\text{Sc}} \left[ \frac{\partial N_i}{\partial x} \frac{\partial C_l}{\partial x} + \frac{\partial N_i}{\partial z} \frac{\partial C_l}{\partial z} \right] d\Omega \\ &= - \int_{\Omega} W_i^3 \left[ u \frac{\partial C_l}{\partial x} + w \frac{\partial C_l}{\partial z} \right] d\Omega + \int_{\Gamma} N_i \frac{\text{Pr } \phi}{\text{Sc}} \frac{\partial C_l}{\partial n} D\Gamma \end{aligned} \quad (34)$$

where the line integral is only calculated along the top boundary when the long-container assumption is made and Eq. (16) is used. In the all-liquid region,  $\bar{C} = C_l$ , and the left-hand side is treated implicitly. In the mushy zone where  $\phi < 1$ , however, we have  $\bar{C} \neq C_l$ , and the second term on the left-hand side is calculated explicitly using the latest values of  $C_l$ .

After interpolating the functions using Eq. (32), all integrals can be evaluated, and three sets of linear algebraic equations result:

$$\mathbf{M}_1 \dot{\mathbf{v}} + \mathbf{K}_1 \mathbf{v} = - \mathbf{Q}_1(\mathbf{v}, \phi, T, C_l) \quad (35)$$

$$\mathbf{M}_2(\phi, C_l) \dot{T} + \mathbf{K}_2(\phi, C_l) T = \mathbf{Q}_2(\mathbf{v}, \phi, T, C_l) \quad (36)$$

$$\mathbf{M}_3 \dot{\bar{C}} + \mathbf{K}_3(\phi) C_l = - \mathbf{Q}_3(\mathbf{v}, \phi, C_l) \quad (37)$$

In the equations above,  $\mathbf{v} = (u_1 w_1 u_2 w_2 \dots u_N w_N)^T$ , where  $N$  is the number of nodes and  $u_i$  and  $w_i$  are the velocity components at the nodes; also,  $\phi = (\phi_1 \phi_2 \dots \phi_N)^T$ ,  $T = (T_1 T_2 \dots T_N)^T$ ,  $C_l = (C_{l1} C_{l2} \dots C_{lN})^T$ , and  $\bar{C} = (\bar{C}_1 \bar{C}_2 \dots \bar{C}_N)^T$ . The mass matrices  $\mathbf{M}_1$  and  $\mathbf{M}_2$  are lumped diagonal matrices (see Refs. [36, 40, and 41] and are given by

$$\begin{aligned}
[m_1]_{ij} &= \int_{\Omega} \text{Pr } N_i d\Omega & i = 2\alpha - 1 & \quad i = j \\
& & i = 2\alpha & \quad i = j \\
[m_1]_{ij} &= 0 & i \neq j & \\
\end{aligned} \tag{38}$$

( $\alpha = 1, 2, \dots, N$ )

$$\begin{aligned}
[m_2(\phi, C_l)]_{ij} &= \int_{\Omega} \left[ \text{Pr} - \frac{L\phi}{C_l} \right] N_i d\Omega & i = j \\
[m_2(\phi, C_l)]_{ij} &= 0 & i \neq j \\
\end{aligned} \tag{39}$$

( $i = 1, 2, \dots, N$ )

The mass matrix  $\mathbf{M}_3$  in the solute concentration is treated consistently and is given by

$$[m_3]_{ij} = \int_{\Omega} \text{Pr } N_i N_j d\Omega \quad i, j = 1, \dots, N \tag{40}$$

The stiffness matrices  $\mathbf{K}_i$  are given by

$$\begin{aligned}
[k_1]_{ij} &= \int_{\Omega} \left\{ \lambda \phi \frac{\partial N_i}{\partial x} \frac{\partial N_j}{\partial x} + \text{Pr} \left[ \frac{\partial N_i}{\partial x} \frac{\partial N_j}{\partial x} + \frac{\partial N_i}{\partial z} \frac{\partial N_j}{\partial z} \right] \right. \\
&\quad \left. + \frac{\text{Pr}\phi}{\text{Da}_x} N_i N_j \right\} d\Omega & i = 2\alpha - 1 \\
& & j = 2\beta - 1 \\
[k_1]_{ij} &= \int_{\Omega} \left\{ \lambda \phi \frac{\partial N_i}{\partial x} \frac{\partial N_j}{\partial z} \right\} d\Omega & i = 2\alpha - 1 \\
& & j = 2\beta \\
[k_1]_{ij} &= \int_{\Omega} \left\{ \lambda \phi \frac{\partial N_i}{\partial x} \frac{\partial N_j}{\partial z} \right\} d\Omega & i = 2\alpha \\
& & j = 2\beta - 1
\end{aligned}$$



$$\begin{aligned}
[k_1]_{ij} = \int_{\Omega} \left\{ \lambda \phi \frac{\partial N_i}{\partial z} \frac{\partial N_j}{\partial z} + \text{Pr} \left[ \frac{\partial N_i}{\partial x} \frac{\partial N_j}{\partial x} + \frac{\partial N_i}{\partial z} \frac{\partial N_j}{\partial z} \right] \right. \\
\left. + \frac{\text{Pr} \phi}{\text{Da}_z} N_i N_j \right\} d\Omega \quad \begin{matrix} i = 2\alpha \\ j = 2\beta \end{matrix} \quad (41) \\
(\alpha, \beta = 1, 2, \dots, N)
\end{aligned}$$

$$\begin{aligned}
[k_2(\phi, C_l)]_{ij} = \int_{\Omega} \left\{ \left[ 1 - \frac{\hat{L}\phi}{\text{Sc} C_l} \right] \left[ \frac{\partial N_i}{\partial x} \frac{\partial N_j}{\partial x} + \frac{\partial N_i}{\partial z} \frac{\partial N_j}{\partial z} \right] \right. \\
\left. + \frac{\hat{L}\phi N_i}{\text{Sc} C_l^2} \left[ \frac{\partial C_l}{\partial x} \frac{\partial N_j}{\partial x} + \frac{\partial C_l}{\partial z} \frac{\partial N_j}{\partial z} \right] \right\} d\Omega \quad (i, j = 1, 2, \dots, N) \quad (42)
\end{aligned}$$

$$\begin{aligned}
[k_3(\phi)]_{ij} = \int_{\Omega} \frac{\text{Pr} \phi}{\text{Sc}} \left[ \frac{\partial N_i}{\partial x} \frac{\partial N_j}{\partial x} + \frac{\partial N_i}{\partial z} \frac{\partial N_j}{\partial z} \right] d\Omega \quad \phi = 1 \\
[k_3(\phi)]_{ij} = 0 \quad \phi < 1 \quad (43) \\
(i, j = 1, 2, \dots, N)
\end{aligned}$$

The vectors  $\mathbf{Q}_i$  are obtained by replacing Eq. (32):

$$\begin{aligned}
[q_1(\mathbf{v}, \phi, T, C_l)]_i = \int_{\Omega} \left\{ \frac{W_i^1}{\phi} \left[ u \frac{\partial u}{\partial x} + w \frac{\partial u}{\partial z} \right] \right. \\
\left. + N_i \phi \cos \theta \text{Pr} \left[ R_T T + \frac{R_S}{\text{Sc}} (C_l - 1) \right] \right\} d\Omega \quad i = 2\alpha - 1 \quad (44)
\end{aligned}$$

$$[q_1(\mathbf{v}, \phi, T, C_l)]_i = \int_{\Omega} \left\{ \frac{W_i^1}{\phi} \left[ u \frac{\partial w}{\partial x} + w \frac{\partial w}{\partial z} \right] + N_i \phi \sin \theta \Pr \left[ R_T T + \frac{R_S}{Sc} (C_l - 1) \right] \right\} d\Omega \quad i = 2\alpha$$

( $\alpha = 1, 2, \dots, N$ )

$$[q_2(\mathbf{v}, \phi, T, C_l)]_i = \int_{\Omega} \left\{ W_i^2 \left[ \frac{\hat{L}}{\Pr C_l} - 1 \right] \left[ u \frac{\partial T}{\partial x} + w \frac{\partial T}{\partial z} \right] + N_i \frac{\bar{L}}{C_l} \frac{\partial I}{\partial t} \right\} d\Omega$$

$$+ \int_{\Gamma} N_i \left[ 1 - \frac{\hat{L}\phi}{Sc C_l} \right] \frac{\partial T}{\partial n} d\Gamma \quad (i = 1, 2, \dots, N) \quad (45)$$

$$[q_3(\mathbf{v}, \phi, T, C_l)]_i = \int_{\Omega} \left\{ \frac{\Pr \phi}{Sc} \left[ \frac{\partial N_i}{\partial x} \frac{\partial C_l}{\partial x} + \frac{\partial N_j}{\partial z} \frac{\partial C_l}{\partial z} \right] + W_i^3 \left[ u \frac{\partial C_l}{\partial x} + w \frac{\partial C_l}{\partial z} \right] \right\} d\Omega$$

$$- \int_{\Gamma} \frac{N_i \Pr \phi}{Sc} \frac{\partial C_l}{\partial n} d\Gamma \quad \phi < 1 \quad (46)$$

$$[q_3(\mathbf{v}, \phi, T, C_l)]_i = \int_{\Omega} W_i^3 \left[ u \frac{\partial \bar{C}}{\partial x} + w \frac{\partial \bar{C}}{\partial z} \right] d\Omega - \int_{\Gamma} \frac{N_i \Pr \phi}{Sc} \frac{\partial \bar{C}}{\partial n} d\Gamma \quad \phi = 1$$

( $i = 1, 2, \dots, N$ )

(47)

The time integration of the systems of ordinary differential equations represented by Eqs. (35)-(37) is performed using a backward implicit scheme. Specifically, discretize the time derivative of a scalar function  $f$  using

$$\dot{f} \cong \frac{f^{m+1} - f^m}{\Delta t}$$

## V. NUMERICAL RESULTS

Calculations were performed for a Pb-10 wt pct Sn alloy under a variety of cooling and boundary conditions. The computational domain is shown in Fig. 1 and consists of a rectangular region of width  $W$  and height  $H_T$ , discretized with a uniform mesh of 20 elements in the  $x$  (horizontal) direction and 30 elements in the  $z$  (vertical) direction. This mesh was selected after several preliminary calculations were performed with different resolutions to assess the sensitivity of the results to the mesh size. The chosen mesh was found to capture all the dynamic features of the flow at a reasonable computation cost, whereas coarser meshes were unable to reveal the formation of the channels. A uniform resolution was used because the locations of channels and regions of macrosegregation were found to be unpredictable.

In all calculations, the channels turned out to be very narrow, comparable to one to several primary dendrite arm spacings (which is also comparable to the solute distribution decay scale  $D/V$ ). The mesh size has to be kept comparable to this scale if proper resolution of the channels is desired. This requirement imposed a limitation on the size of the domain, in order not to make a single computation excessively expensive. Fortunately, all the effects associated with channel creation and growth could be observed in calculations even though the domains were rather small. Furthermore, when different sizes were used, it was found that channels developed under the same thermal conditions irrespective of size of domain.

A reference length scale  $H = 300 \mu\text{m}$  was chosen for all the calculations. The following nondimensional parameters were also used:

$$Ra_T = 3.4 \times 10^{-3}$$

$$Ra_s = 1.86 \times 10^4$$

$$Pr = 2.3 \times 10^{-2}$$

$$Sc = 8.23 \times 10^1$$

$$L/\hat{c}GH = 7.5 \times 10^2$$

The reference time,  $\tau$ , was 0.65 s, and the reference velocity,  $U$ , was 27 mm·s<sup>-1</sup>. The reference temperature was taken to be the freezing point of the Pb-10 wt pct Sn alloy ( $T_0 = 577$  K), and the reference concentration was  $C_0 = 10$  wt pct Sn.

The first calculation considers a container of width  $W = 10$  mm with a domain height of  $H_T = 20$  mm. Zero tangential stress and zero vertical velocity are imposed on the top boundary ( $z = H_T$ ), and no-slip at the other three boundaries. The alloy is initially all liquid of concentration  $C_0 = 10$  wt pct Sn, and has a linear temperature distribution varying from  $T_0$  (the melting point) at the bottom boundary to  $T_0 + GH_T$  at the top boundary, with  $G = 1000$  K·m<sup>-1</sup>. The side walls are insulated, and a vertical gradient of  $\partial T/\partial z = G$  is imposed at the top boundary. A time dependent boundary condition is prescribed at the bottom of the form:

$$T(x,0,t) = T_0 - rt$$

where  $r$  is the cooling rate (0.0783 K s<sup>-1</sup>). With this value of  $r$ , the initial solidification rate was approximately 0.042 mm s<sup>-1</sup>. The values of the cooling rate,  $r$ , and the thermal gradient,  $G$ , were selected from the thermal history of ingots of Pb-10 Sn alloy that exhibited channel segregates in the experiments of Sarazin and Hellawell [7].

The thermodynamic and transport properties used in the calculations are given in Table I. The functions used for the anisotropic permeability are given in the Appendix.

Table I.

Thermodynamic and Transport Properties Used for Calculations  
in Pb-10 wt pct Sn. Taken from Ref. [33].

Property
Reference concentration ( $C_0$ ), 10 wt pct Sn
Reference temperature ( $T_0$ ), 577 K
Equilibrium partition ratio ( $k$ ), 0.31
Melting point of lead ( $T_M$ ), 600 K
Slope of liquidus ( $m$ ), $-2.33 \text{ K (wt pct)}^{-1}$
Density [ $\rho_0 = \rho(C_0, T_0)$ ], $1.01 \times 10^4 \text{ kg}\cdot\text{m}^{-3}$
Thermal expansion coefficient ( $\beta_T$ ), $1.2 \times 10^{-4} \text{ K}^{-1}$
Solutal expansion coefficient ( $\beta_C$ ), $5.15 \times 10^{-3} \text{ (wt pct)}^{-1}$
Kinematic viscosity ( $\nu_0$ ), $2.47 \times 10^{-7} \text{ m}^2 \text{ s}^{-1}$
Latent heat ( $L$ ); $\text{kJ kg}^{-1}$ :
At ( $C_0, T_0$ ), 26
At ( $C_E, T_E$ ), 56
Used in calculation, 37.6
Heat capacity ( $\hat{c}$ ); $\text{kJ kg}^{-1} \text{ K}^{-1}$ :
Liquid at ( $C_0, T_0$ ), 0.161
Solid at ( $C_E, T_E$ ), 0.173
Used in calculation, 0.167
Thermal conductivity ( $\kappa$ ); $\text{kW m}^{-1} \text{ K}^{-1}$ :
Liquid at $C_0, T_0$ , 0.0167
Mixture at ( $C_E, T_E$ ), 0.0198
Used in calculation, 0.0182
Thermal diffusivity ( $\alpha = \kappa/\rho_0\hat{c}$ ), $1.1 \times 10^{-5} \text{ m}^2 \text{ s}^{-1}$
Solutal diffusivity ( $D$ ), $3 \times 10^{-9} \text{ m}^2 \text{ s}^{-1}$

Figure 2 shows calculated results after 3 min. The contours of equal fraction liquid (Fig. 2a) show a very narrow region of high fraction liquid at the center of the casting, indicating the presence of a freckle or a channel. Note that the mesh size is not sufficiently small to resolve an all-liquid jet. Nevertheless, it can be seen from the streamlines (Fig. 2b) that the flow is upward within the channel and extends into the bulk liquid as a column of rising fluid. Although the streamlines penetrate into the mushy zone, the strength of the

convection rapidly diminishes within the mushy zone where the permeability is low.

Figure 2c shows that the fluid within the channel is richer in solute than the surrounding fluid.

A more detailed view of a freckle is obtained in the next example (Fig. 3), where a very small container of dimensions 2.5 mm by 4.5 mm was used, together with a slower initial solidification rate of  $V = 0.0139 \text{ mm}\cdot\text{s}^{-1}$ . The width of the channel is approximately equal to the reference length scale ( $H = 0.3 \text{ mm}$ ). Note the steep gradient of fraction liquid on the channel walls, indicating that the channel is surrounded by a region of low volume fraction liquid. The flow is upward inside the channel, and two cells have developed next to the mold walls (Fig. 3b), where there is also upward flow and a higher than normal fraction of liquid.

In the examples of Figs. 2 and 3 the channels in the centers were induced by introducing an initial perturbation in the concentration of the melt along the vertical centerline and letting the system evolve thereafter. The form of the perturbation was

$$C_l = 1.01 C_0 \quad \text{for } x = W/2.$$

In this way, an initial upward flow at the center of the container is established. The situation is similar to experiments done by Sample and Hellawell [8] in  $\text{NH}_4\text{Cl-H}_2\text{O}$ , in which they created channels in the mushy zone by inducing an upward flow in the liquid just ahead of the dendritic tips by suction up through a capillary tube.

In the next calculation no perturbation is introduced, and the system is left to evolve undisturbed. The width of the mold is 5 mm, and the height of the computational domain is  $H_T = 10 \text{ mm}$ . No-stress conditions are imposed on the top boundary, simulating an

infinitely high column of liquid above the mushy zone. The cooling rate is  $r = 0.0167 \text{ K s}^{-1}$ , corresponding to an initial solidification rate of  $V = 0.0139 \text{ mm s}^{-1}$  ( $50 \text{ mm h}^{-1}$ ). All other boundary conditions were the same as in the examples of Figs. 2 and 3. The results of this calculation are given in Figs. 4 and 5.

After 2 minutes, two channels begin to form (Fig. 4a) at locations corresponding to zones of upward flow of four convective cells (Fig. 5a). The channels, however, do not keep growing upward, but they turn toward the sides and continue to grow along the walls of the mold (Figs. 4b through d), following the path of upward convective flow (Figs. 5b through d). An additional channel can be seen in Figs. 4c and 5c that appears as a pocket in the upper part of the mushy zone (indicated by arrows). However, the channel rapidly closes leaving a pocket of liquid surrounded by a dendritic network with a greater volume fraction of solid (Fig. 4d). Abrupt transitions in the volume fraction of liquid surrounding the pocket or the channels are indicated by the dark regions of closely packed contour lines.

A plot of total concentration of the partially solidified casting (Fig. 6) shows that within the mushy zone there is obvious positive macrosegregation in the channels along the wall and within the now isolated pocket.

The effect of heat flow between the casting and the furnace is studied in the next example. The two calculations are shown in Figs. 7a and b for a domain with a width of 5 mm and a no-stress top boundary at 10 mm as in the previous example. The cooling rate, however, is only  $8.33 \times 10^{-3} \text{ K s}^{-1}$ . In Fig. 7a heat is also extracted from the casting by imposing a temperature gradient  $|\partial T/\partial x| = 0.1 \text{ K mm}^{-1}$  at the side walls. Except for channels at the walls, the mushy zone adopts a concave shape toward the bulk liquid. Only

channels at the walls develop and no interior channels or pockets are observed. In Fig. 7b, heat is added to the casting by imposing  $|\partial T/\partial x| = 0.3 \text{ K mm}^{-1}$  at the side walls and by specifying a lower temperature at the center of the base (increasing linearly toward the sides). Apart from the channels, the overall shape of the growth front is convex to the liquid; now channels develop in the interior of the container, although the channels at the walls still remain.

It is evident from the above example that channels tend to develop in the leading part of the growth front. This fact has been observed in experiments with  $\text{NH}_4\text{Cl-H}_2\text{O}$  mixtures [5,8]. Copley *et al.* [5] varied the configuration of their bottom chill so as to make the growth front either concave or convex to the liquid. When it was concave, channels in the  $\text{NH}_4\text{Cl-H}_2\text{O}$  system tended to form on the outside, and when it was convex the channels were prevalent in the center. Similar results were obtained by Sample and Hellawell [8], who tilted the ingots.

Based on the calculations presented, herein, it is also evident that there is a strong tendency for freckles to form at the walls of the mold. In order to investigate why a wall might be an attractive place for freckling, a numerical experiment was done using the same domain with insulated walls and prescribing a zero horizontal velocity along the vertical center line (*i.e.*,  $x = W/2$ ). It is observed in Fig. 8a that a freckle forms at the center of the casting and keeps growing, supported by a column of upward flowing liquid, in a similar way as the channels along the walls (Fig. 8b). Two additional channels develop at positions intermediate between the center and the walls, but they do not persist (Fig. 8c) because they face an unfavorable flow pattern in the liquid zone. It is important to remark that in this



example the upward flow at the center of the container is not induced by an initial perturbation, but it arises naturally as a consequence of restricting the horizontal movement of fluid. A similar result was obtained by prescribing a highly anisotropic permeability ( $K_x = 10^{-3} K_z$ ) along the vertical center line in the mushy zone, showing that a restriction to horizontal convection in the mushy zone can sustain a column of upward flow in the liquid.

## VI. DISCUSSION

The results presented herein illustrate some of the most common effects observed in experiments on freckles. Several remarks can be made that are based upon the results.

1. The convection starts immediately, as soon as the liquid next to the base of the container begins to solidify. The convection cells nucleate near the advancing solidification front (*i.e.*, at the tips of the dendrites). From the calculated temperatures and concentrations in this region, it is found that the vertical density gradient is positive there, *i.e.*, it is gravitationally unstable.
2. As the solidification proceeds, the convective cells do not keep organized. The flow pattern changes continually, driven almost entirely by the solute concentration field. The isotherms are practically flat because of the low Prandtl number. The convection in the bulk liquid penetrates deeply into the mushy zone, although the velocities decrease by 2 or 3 orders of magnitude below the upper 20 pct of the mushy zone.
3. The first channels begin to form in regions of upward flow, between two convective cells (*e.g.*, Fig. 2a). Because the solute concentration in the liquid is

higher at the bottom of the casting, the upward flow transports solute-rich liquid to the tips of the dendrites, decreasing the freezing point. Therefore, the growth front advances more slowly in regions where there is upward flow, it distorts, and a channel begins to develop backward from the tips toward the bottom of the mushy zone. This process is helped further by remelting of already existing solid in the mushy zone. The diffusion of solute is too slow to spread away from the column of rising solute-rich liquid, so remelting occurs in order to decrease the solute concentration in the liquid back to an equilibrium value that corresponds to the local temperature. In other words, without remelting a volume of rising interdendritic liquid is unable to maintain its thermodynamic equilibrium because heat diffuses much faster than the solute; remelting counteracts this by diluting the liquid with respect to the solute.

4. The larger concentration of solute in a column of rising liquid tends to keep it rising because of buoyancy and double diffusion effects (assuming that the solute is lighter than the solvent, e.g. Sn in Pb-rich alloys). This keeps the channel growing vertically, until the pattern of convection changes, and the column of liquid emerging from the channel is disturbed. The flow change is caused by accumulation of solute in a nearby place, creating a competing channel. The old channel deviates from its vertical trajectory, induced by the upward flow at the new position, and eventually merges with the new channel or closes before reaching it, forming a pocket or streak.

5. In most of our calculations, we observe a strong accumulation of solute at the walls of the mold, leading to long, well defined channels that dominate the flow and prevent other similar channels from growing in the interior of the casting. Channels that develop in the interior of the casting, either naturally or induced by a perturbation, are eventually absorbed by the channels at the walls. This predominance of freckles at the surface of the mold has been observed in Ni-based alloys [6]. The solute accumulates next to the walls because of the limitation of lateral transport; *i.e.*, it is harder to remove solute away from the wall because the horizontal component of the velocity is small. For high solidification rates ( $\sim 4.2 \times 10^{-2} \text{ mm s}^{-1}$ ) the formation of channels at the walls can be delayed or prevented, because not enough time is allowed for solute accumulation.
6. Long, vertical channels, similar to the ones at the surface of the casting, can be obtained in the interior if a restriction to lateral convection is introduced (Fig. 8). The purpose is to provoke an accumulation of solute that can sustain the channel growth. Such an accumulation could occur in regions of high anisotropy in the mushy zone ( $K_x \ll K_z$ ), as might be the case in grain boundaries, dendrite misalignments or other defects in the dendritic network of the mushy zone. Another mechanism that can favor the formation of long interior channels is the deposit of dendrite debris, produced by remelting or erosion of the dendrite arms, along the channel sides. This phenomenon has been observed in the  $\text{NH}_4\text{Cl-H}_2\text{O}$  system [5]. The debris grow as small randomly oriented grains that

entangle with the sides of the channel and reduce the horizontal permeability. In effect, the solute is confined to the channel. Because this decreases the lateral feeding of liquid, the channel activity is significant only in the neighborhood of the dendrite tips, and the liquid in the bottom part of the channel is essentially stagnant.

## VII. CONCLUSIONS

A mathematical model of solidification of dendritic alloys with thermosolutal convection has been presented. The solidification is initiated from an all-liquid state, and the dendritic zone is allowed to grow as the volume fraction of liquid in the mushy zone adjusts according to local thermodynamic equilibrium conditions. Calculations were performed for the vertical solidification of a Pb-10 wt pct Sn alloy, with the following results:

1. Channels form during the growth of the mushy zone.
2. The shape of the channels vary from small pockets or short streaks of interdendritic liquid to long vertical penetrations.
3. The formation of a channel occurs near the leading part of the growth front.
4. The liquid within the channels is enriched in solute.
5. The channels form in regions of upward flow. The mushy zone grows around the columns of rising liquid, forming the channels backward from the tips of the dendrites toward the bottom of the mushy zone. Remelting also takes place.
6. The convection is driven mainly by the solute field. Zones of solute accumulation are potential starters of channels.

7. Channels can be induced by establishing a column of upward flow in the bulk liquid, by introducing a restriction to the horizontal convection in the mushy zone, or by enhancing the vertical convection.
8. There is a strong preference for channels to form at the mold walls.

## VIII. OTHER ACCOMPLISHMENTS

The major emphasis in the research program was to model thermosolutal convection during the dendritic solidification of binary alloys, and the results of this effort are given in the preceding chapters. In this chapter, we summarize other accomplishments pertaining to the subject research. Details are not given here, but publications resulting from the work may be consulted.

The two most important publications on the model, itself, are given as References 33 and 46. The former appears in *Metallurgical Transactions*, which is widely read by the materials community, and the latter appears in *Numerical Heat Transfer*, where the mathematical details pertaining to the finite element algorithms and computational strategy peculiar to the solidification scenario are given. Our results were also presented at several conferences, all of which resulted in publications (References 47-50).

In setting up the conservation equations for the mushy zone, we found it necessary to derive the momentum equation [30] and to numerically test our calculations [31] and contrast them to results calculated from a form of the momentum equation used by other researchers. This was necessary because in analyzing dendritic solidification, the mushy zone is modeled as a porous medium with a spatially varying fraction of liquid, unlike the uniform porosity in

most porous media. There were also fundamental issues, which had to be addressed, in both the energy equation and the solute conservation equation, resulting in the publication of Reference 51.

## APPENDIX

### Functions Used for Permeability

We assume directional solidification with dendritic columnar grains. The permeability is anisotropic with components  $K_x$  and  $K_y$  for flow perpendicular to the columnar dendrites and flow parallel to the columnar dendrites, respectively.

In this work thermal conditions, corresponding to ingots studied by Sarazin and Hellawell [7], were used in the simulations, so we also used their reported primary dendrite arm spacing of 300  $\mu\text{m}$ . Lacking a value for secondary dendrite arm spacing, Eq. [30] from Poirier [42] was selected for  $K_x$ ; it is

$$K_x = 7.08 \times 10^{-16} d_1^{2.08} \phi^{3.32} \quad [\text{A1}]$$

with  $K_x$  in  $\text{m}^2$  and  $d_1$  in  $\mu\text{m}$ .

Equation [A1] is based on a regression analysis of empirical data that cover the scope  $0.19 \leq \phi \leq 0.66$  and  $144 \leq d_1 \leq 420 \mu\text{m}$ .

For the regime with  $\phi > 0.66$ , we use

$$\frac{K_x}{d_1^2} = a_0 + a_1 \left[ \frac{\phi}{1 - \phi} \right]^{1/4} \quad [\text{A2}]$$

where  $a_0 = -5.955449 \times 10^{-2}$  and  $a_1 = 5.652925 \times 10^{-2}$ .

Equation [A2] and the coefficients were determined by a linear regression of results given in Tables 1 and 2 of Sangani and Acrivos [43] for  $0.6 \leq \phi < 0.95$ , and calculated with their Eqs. (17) and (25) for  $0.95 \leq \phi \leq 0.99$ . Sangani and Acrivos [43] studied the slow flow past square arrays and triangular arrays of circular cylinders; Eq. [A2] is a compromise between the square array and the triangular array.

#### Flow Parallel to Columnar Dendrites

The empirical data are listed in Reference 42; the scope is  $0.17 \leq \phi \leq 0.61$  and  $28 \leq d_1 \leq 420 \mu\text{m}$  for which the following empirical relationship was determined:

$$\frac{K_z}{d_1^2} = 3.75 \times 10^{-4} \phi^2 \quad [\text{A3}]$$

There are no empirical data for  $\phi > 0.61$ , so we use the results of Drummond and Tahir [44] and Ganesan *et al.* [45].

Drummond and Tahir [44] derived equations for laminar flow parallel to regular arrays of circular cylinders. Based upon values of drag forces given in their Table 5 and their equations for small values of  $(1 - \phi)$ , permeabilities were calculated.

Ganesan *et al.* [45] calculated the permeability for flows parallel to primary dendrites based upon actual microstructures. Their results agree very well with the results derived from Drummond and Tahir for  $g_L \geq 0.55$ . Therefore, when  $\phi > 0.61$  we use an equation given by them; it is

$$\frac{K_z}{d_1^2} = a \left[ \ln (1 - \phi)^{-1} - b + 2(1 - \phi) - \frac{(1 - \phi)^2}{2} \right] \quad [\text{A4}]$$

where  $a$  and  $b$  are constants that depend on the array of the cylinders. In this work, we selected average values for triangular and square arrays:  $a = 0.07425$   $b = 1.487$ .

#### REFERENCES

1. M. McLean: *Directionally Solidified Materials for High Temperature Service*, The Metals Society, London, 1983, pp. 1-8.
2. R. J. McDonald and J. D. Hunt: *Trans. TMS-AIME*, 1969, vol. 245, pp. 1993-97.
3. W. D. Bennon and F. P. Incropera: *Metall. Trans. B*, 1987, vol. 18B, pp. 611-16.
4. R. J. McDonald and J. D. Hunt: *Metall. Trans.*, 1970, vol. 1, pp. 1787-88.
5. S. M. Copley, A. F. Giamei, S. M. Johnson and M. F. Hornbecker: *Metall. Trans.*, 1970, vol. 1, pp. 2193-2204.
6. A. F. Giamei and B. H. Kear: *Metall. Trans.*, 1970, vol. 1, pp. 2185-91.
7. J. R. Sarazin and A. Hellawell: *Metall. Trans. A*, 1988, vol. 19A, pp. 1861-71.
8. A. K. Sample and A. Hellawell: *Metall. Trans. A*, 1984, vol. 15A, pp. 2163-73.
9. V. Laxmanan, A. Studer, L. Wang, J. F. Wallace and E. A. Winsa: NASA Technical Memorandum 89885, presented at the Low Gravity Science Seminar Series, University of Colorado, Boulder, CO, Feb. 17, 1986.
10. A. C. Fowler: *IMA J. Appl. Math.*, 1985, vol. 35, pp. 159-74.
11. R. Mehrabian, M. A. Keane and M. C. Flemings: *Metall. Trans.*, 1970, vol. 1, pp. 3238-41.



12. M. Simpson, M. Yerebakan and M. C. Flemings: *Metall. Trans. A*, 1985, vol. 16A, pp. 1687-89.
13. J. C. Heinrich, S. Felicelli and D. R. Poirier: *Comp. Meth. Appl. Mech. Eng.*, 1991, to be published.
14. N. Streat and F. Weinberg: *Metall. Trans.*, 1972, vol. 3, pp. 3181-84.
15. M. J. Stewart and F. Weinberg: *J. Cryst. Growth*, 1972, vol. 12, pp. 217-27.
16. J. C. Heinrich, S. Felicelli, P. Nandapurkar and D. R. Poirier: *Metall. Trans. B*, 1989, vol. 20B, pp. 883-91.
17. M.C. Flemings and G.E. Nereo: *Trans. Metall. Soc. AIME*, 1967, vol. 239, pp. 1449-1461.
18. M.C. Flemings, R. Mehrabian, and G.E. Nereo: *Trans. Metall. Soc. AIME*, 1968, vol. 242, pp. 41-49.
19. M.C. Flemings and G.E. Nereo, *Trans. Metall. Soc. AIME*, 1968, vol. 242, pp. 50-55.
20. R. Mehrabian, M. Keane, and M.C. Flemings: *Metall. Trans.*, 1970, vol. 1, pp. 1209-1220.
21. S. Kou, D.R. Poirier, and M.C. Flemings: *Metall. Trans. B*, 1978, vol. 9B, pp. 711-719.
22. A.L. Maples and D.R. Poirier: *Metal. Trans. B*, 1984, vol. 15B, pp. 163-172.
23. S.D. Ridder, S. Kou, and R. Mehrabian: *Metall. Trans. B.*, 1981, vol. 12B, pp. 435-447.
24. W.D. Bennon and F.P. Incropera: *Int. J. Heat Mass Trans.*, 1987, vol. 30, pp. 2161-2170.

25. W.D. Bennon and F.P. Incropera: *Int. J. Heat Mass Trans.*, 1987, vol. 30, pp. 2171-2187.
26. W.D. Bennon and F.P. Incropera: *Numer. Heat Trans.*, 1988, vol. 13, pp. 277-296.
27. C. Beckermann and R. Viskanta: *Phys. Chem. Hydrodyn.*, 1988, vol. 10, pp. 195-213.
28. C. Beckermann and R. Viskanta: *Int. J. Heat Mass Trans.*, 1988, vol. 31, pp. 35-46.
29. S.D. Felicelli: Ph.D. dissertation, University of Arizona, Tucson, 1991.
30. S. Ganesan and D.R. Poirier: *Metall. Trans. B*, 1990, vol. 21B, pp. 173-181.
31. P. Nandapurkar, D.R. Poirier, and J.C. Heinrich: *Numer. Heat Transfer, Part A*, 1991, vol. 19, pp. 297-311.
32. M.C. Flemings, *Solidification Processing*, McGraw-Hill, New York, 1974, pp. 77-83, 160-167.
33. S.D. Felicelli, J.C. Heinrich, and D.R. Poirier: *Metall. Trans. B*, 1991, vol. 22B, pp. 847-859.
34. R.S. Marshall, J.C. Heinrich, and O.C. Zienkiewicz: *Numer. Heat Transfer*, 1978, vol. 1, pp. 315-330.
35. J.C. Heinrich and R.S. Marshall: *Comput. Fluids*, 1981, vol. 9, pp. 78-83.
36. J.C. Heinrich and C.-C. Yu, *Comput. Meth. Appl. Mech. Eng.*, 1988, vol. 69, pp. 1-27.
37. J.T. Oden: *Finite Elements in Fluids*, vol. 4, R.H. Gallagher *et al.*, editors, John Wiley, New York, 1980, pp. 305-318.
38. J.L. Sohn and J.C. Heinrich: *Int. J. Numer. Meth. Eng.*, 1990, vol. 30, pp. 349-361.

39. J.C. Heinrich and B. D  n  : *The Finite Element Method in the 1990's*, E. O  ate *et al.*, editors, Springer-Verlag, Berlin, 1991, pp. 465-476.
40. J.C. Heinrich: *Int. J. Numer. Meth. Eng.*, 1984, vol. 20, pp. 447-464.
41. J.C. Heinrich: *Comput. Meth. Appl. Mech. Eng.*, 1988, vol. 69, pp. 65-88.
42. D.R. Poirier: *Metall. Trans. B*, 1987, vol. 18B, pp. 245-56.
43. A.S. Sangani and A. Acrivos: *Int. J. Multiphase Flow*, 1982, vol. 8, pp. 193-206.
44. J.E. Drummond and M.I. Tahir: *Int. J. Multiphase Flow*, 1984, vol. 10, pp. 515-40.
45. S. Ganesan, C.L. Chan and D.R. Poirier: *Mater. Sci. Eng.*, 1992, vol. A151, pp. 97-105.
46. S.D. Felicelli, J.C. Heinrich and D.R. Poirier: *Numer. Heat Transfer, Part B*, 1993, vol. 23, 461-481.
47. J.C. Heinrich, S.Felicelli and D.R. Poirier: *Comput. Meth. Appl. Mech. Eng.*, 1991, vol. 89, pp. 435-461.
48. D.R. Poirier and J.C. Heinrich: in *Topics in Heat Transfer*, 1992, vol. II, M. Touer *et al.*, editors, ASME, New York, NY, pp. 167-174.
49. S.D. Felicelli, J.C. Heinrich and D.R. Poirier: *Latin American Appl. Res.*, 1991, vol. 21, pp. 209-216.
50. J.E. Crempien-Laborie, J.C. Heinrich and D.R. Poirier: *Supercomputer*, 1993, vol. X, pp. 15-23.
51. D.R. Poirier, P.J. Nandapurkar and S. Ganesan: *Metall. Trans. B*, 1991, vol. 22B, pp. 889-900.

## ACKNOWLEDGMENTS

This was supported by the National Aeronautics and Space Administration under Grant NAG 3-1060. Computational support on a Cray supercomputer was provided by Cray Research, Inc., Eagan, MN, and the San Diego Supercomputer Center. The authors were particularly privileged to have worked with Dr. S. Felicelli, now at Centro Atomico Bariloch in Argentina. This report is largely based on his Ph.D. dissertation and many related publications. Dr. P.J. Nandapurkar, now at DOW USA in Freeport, TX, and Professor J.E. Crempien of the University of Concepción in Chile, also played important roles in the grant.

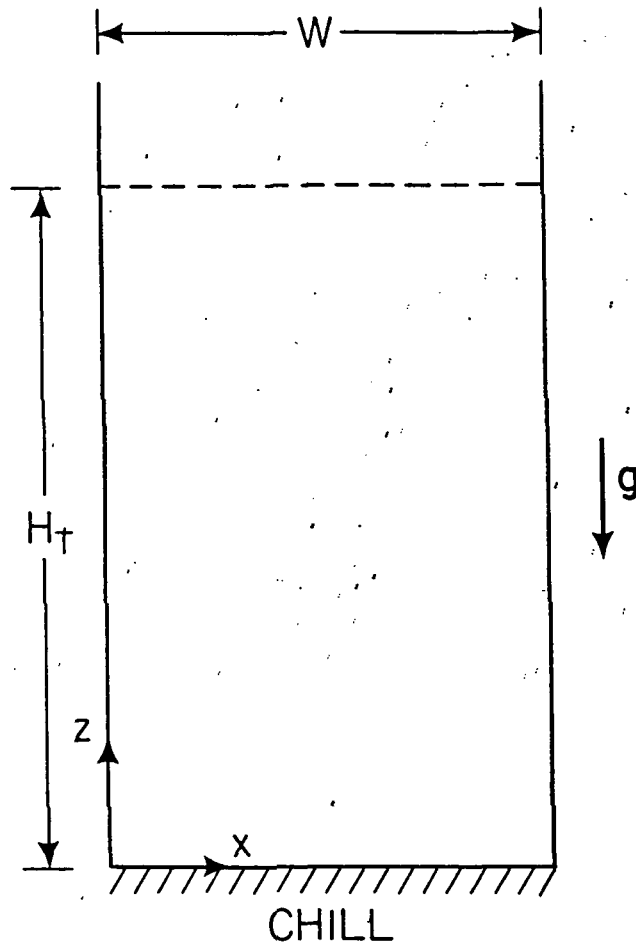


Fig. 1--Domain and coordinate system for vertical solidification.



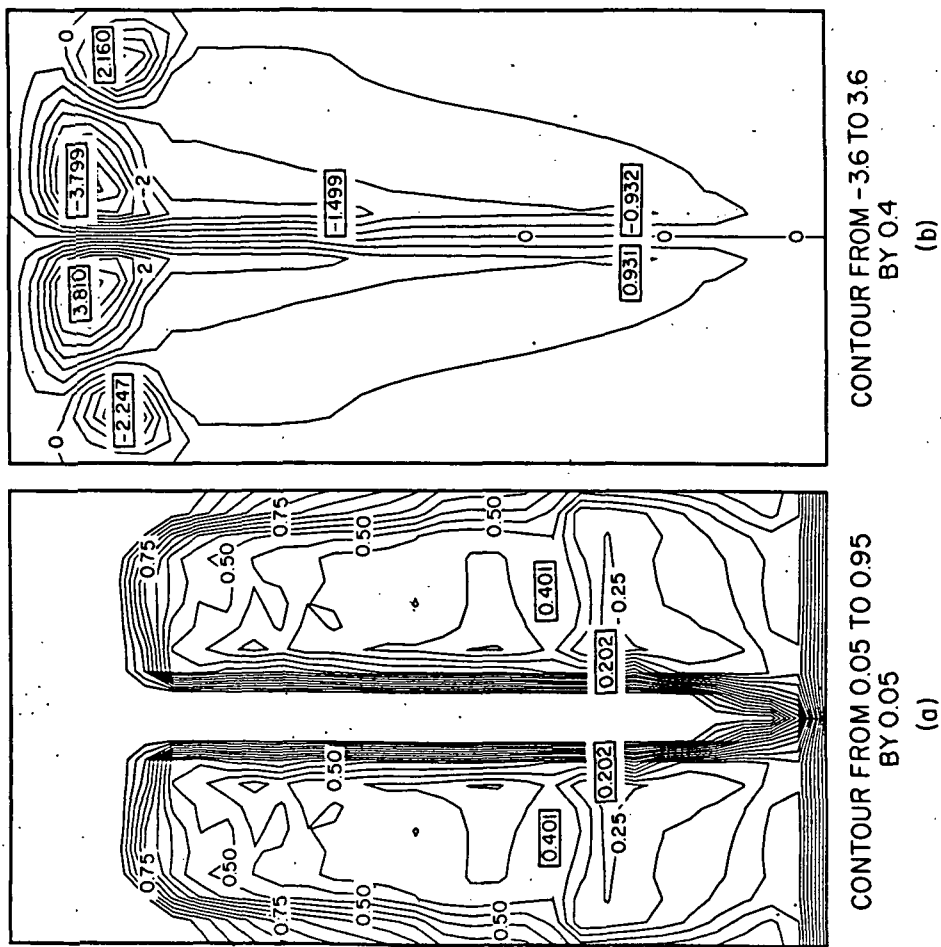


Fig. 3--Calculation in a small domain showing closer details of (a) fraction liquid and (b) streamlines at 10 min.

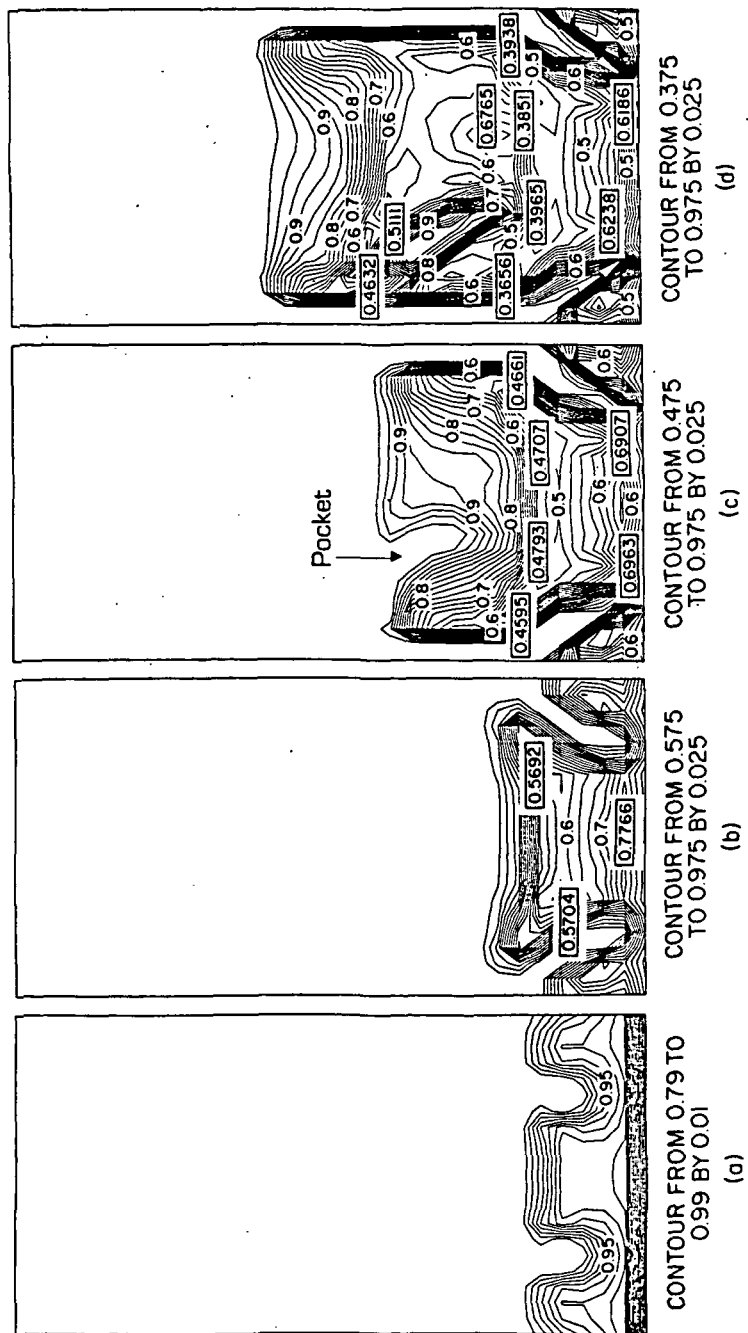
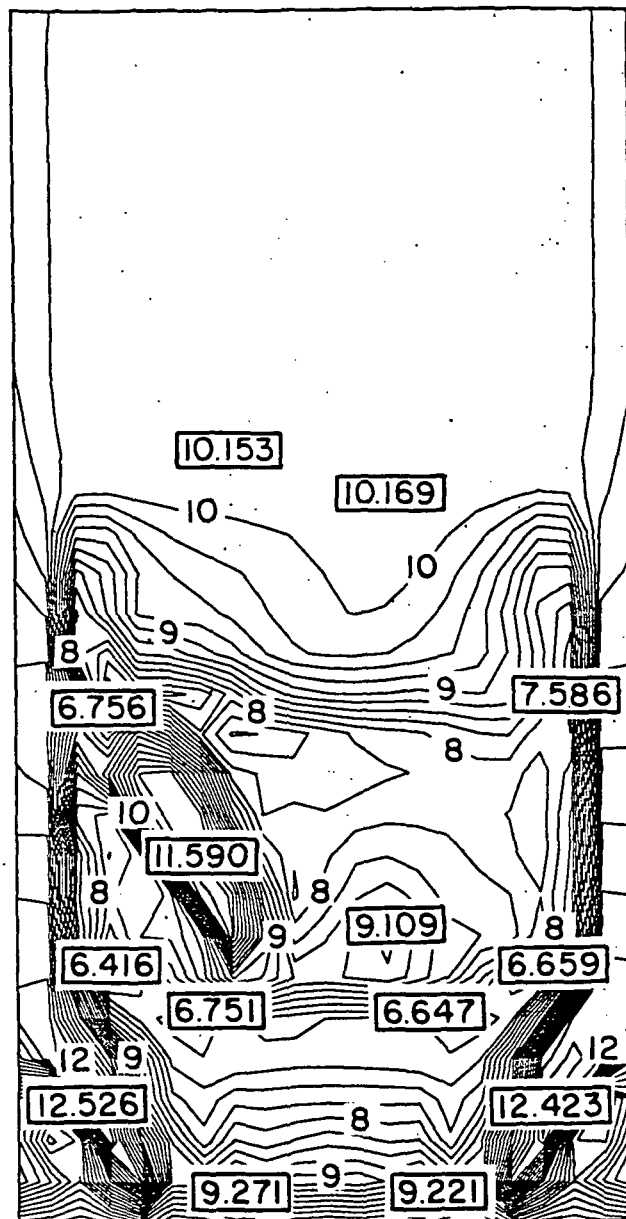


Fig. 4--Formation and propagation of channels during growth of the mushy zone: fraction liquid at (a) 2 min, (b) 3 min, (c) 5 min, and (d) 7 min.







CONTOUR FROM 6.5 TO 12.5  
BY 0.25

Fig. 6--Total concentration (weight percent in solid plus liquid) showing macrosegregation in channels, corresponding to Figs. 4d and 5d (7 min).

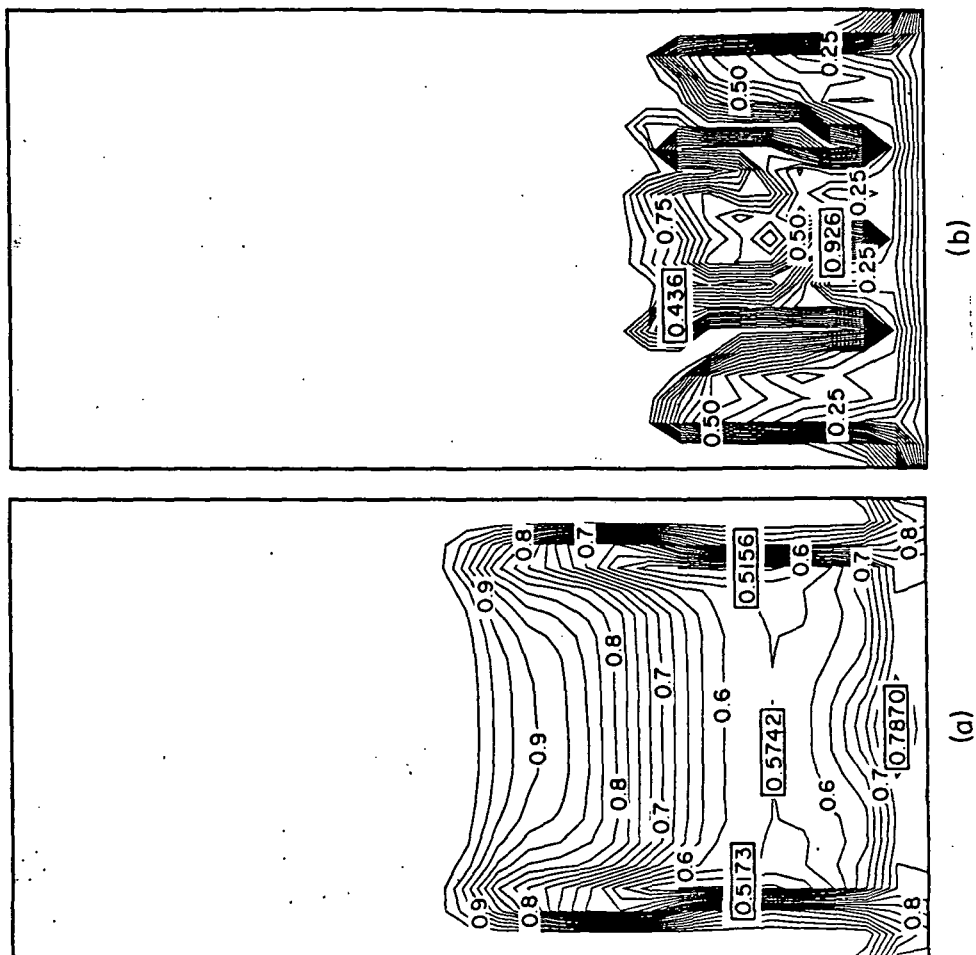


Fig. 7--Channel locations by volume fraction liquid in a (a) concave (5 min) and (b) convex (20 min) mushy zone.

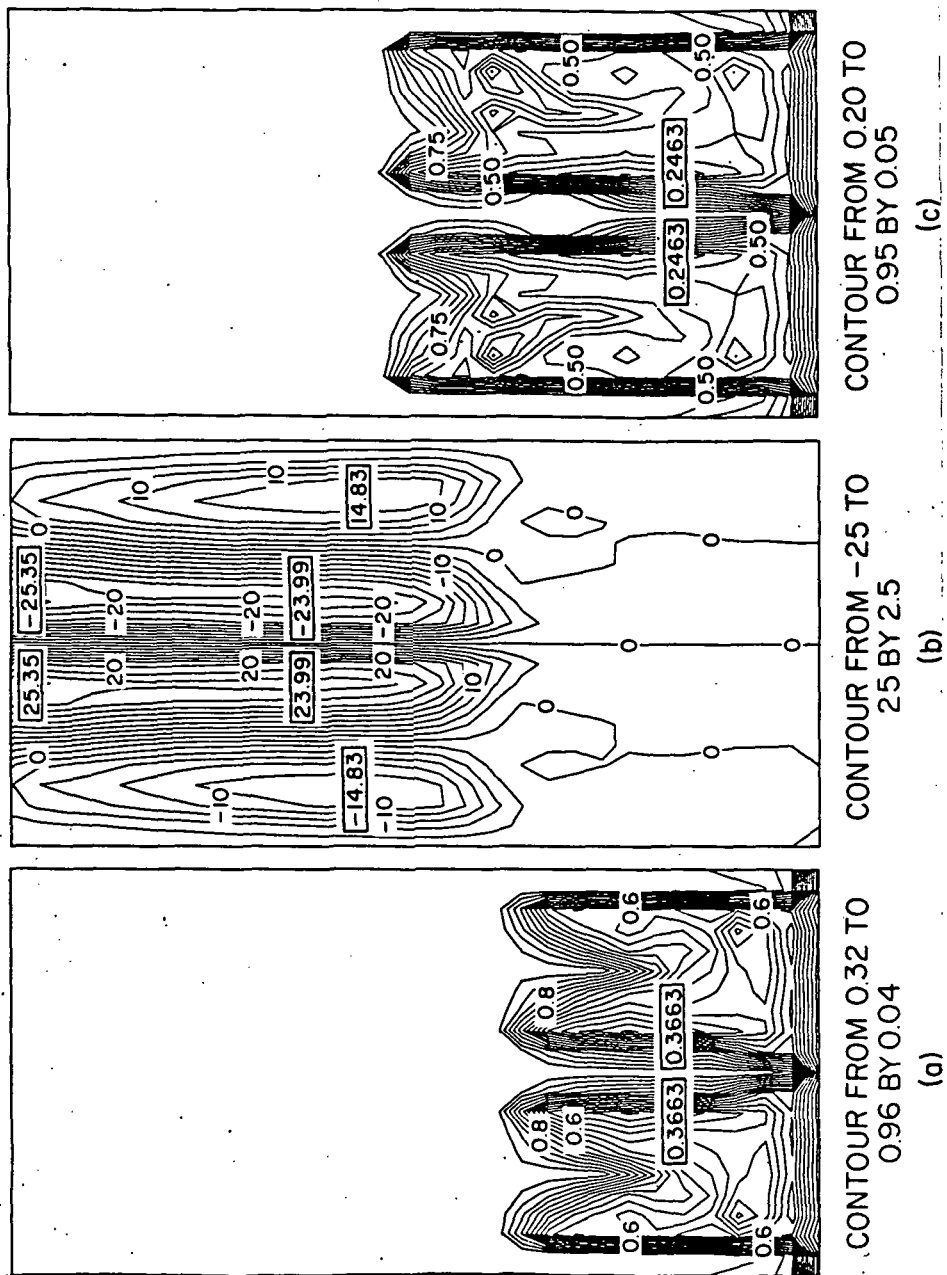


Fig. 8--Channel at the center of the casting formed by inserting a restriction on horizontal convection: (a) contours of fraction liquid at 10 min, (b) stream functions at 10 min, and (c) contours of fraction liquid at 15 min.